Chinese Journal of Structural Chemistry

ARTICLE

Bi and S Co-doping g-C_3N_4 to Enhance Internal Electric Field for Robust Photocatalytic Degradation and H_2 Production

Yan Hu[1], Xibao Li[1,2]*, Weiwei Wang[1], Fang Deng[2]*, Lu Han[3]*, Xiaoming Gao[4], Zhijun Feng[1], Zhi Chen[1], Juntong Huang[1], Fanyan Zeng[1] and Fan Dong[5]

[1]*School of Materials Science and Engineering, Nanchang Hangkong University, Nanchang 330063, China*

[2]*Key Laboratory of Jiangxi Province for Persistent Pollutants Control and Resources Recycle, Nanchang Hangkong University, Nanchang 330063, China*

[3]*School of Materials and Metallurgy, University of Science and Technology, Anshan, Liaoning 114051, China*

[4]*Department of Chemistry and Chemical Engineering, Shaanxi Key Laboratory of Chemical Reaction Engineering, Yan'an University, Yan'an 716000, China*

[5]*Institute of Fundamental and Frontier Sciences, University of Electronic Science and Technology of China, Chengdu 611731, China*

ABSTRACT By adjusting the type and proportion of doping elements in the g-C_3N_4-based photocatalyst, the internal electric field (IEF) strength of the semiconductor can be regulated. This can effectively enhance the driving force of charge separation in the photocatalytic process. It is found that the introduction of appropriate concentration of Bi and S into the skeleton structure of g-C_3N_4 can achieve efficient degradation of tetracycline (TC) and other pollutants in the liquid environment and excellent photocatalytic H_2 evolution performance (1139 μmol·L^{-1}·h^{-1}). Since the prepared samples have similar crystal structures, the relative strength of IEF can be calculated. It can be used as the basis for adjusting the IEF strength of g-C_3N_4-based semiconductor by element doping. In addition, the Bi and S co-doped g-C_3N_4 samples after solvothermal reflux show good chemical stability and can reduce the nanostructure defects caused by co-doping of heteroatoms, thus it provides a novel solution for the construction of g-C_3N_4-based dual-function photocatalyst with high activity and stability.

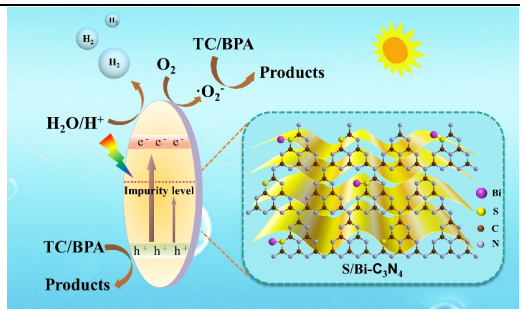

Keywords: photocatalysis, g-C_3N_4, co-doping, IEF strength, antibiotic

n INTRODUCTION

It is well known that the internal electric field (IEF) as an electric field formed spontaneously inside the semiconductor material is not limited by the material form, and there is no additional energy consumption.[1-6] Recently, studies have shown that emerging IEF engineering can play an important role in the field of photocatalysis.[7-10] It can not only improve the efficiency of charge carrier separation in single catalysts, but also induce the diffusion and migration of carriers between the contact interfaces of composite catalysts.[11-14] However, IEF is immobilized and easily saturated, so its ability to promote photocatalysis is still limited. In response to this, Zhu et al.[15] proposed several strategies to enhance IEF based on the generation pathway and the mechanism of the action of IEF: I. The structure of the unit cell can be changed to enhance IEF; II. High electronegativity elements can be doped to enhance IEF; III. Heterojunction can be constructed to enhance interfacial IEF; IV. IEF can be improved under suitable external field conditions. It is worth noting that in single-component catalysts, in addition to adjusting the local IEF in the unit cell by methods such as crystal plane engineering,[16] a small amount of external heteroatoms can also be introduced to change the charge distribution in the bulk phase of catalyst, thereby generating electron acceptor center and electron donor center, which eventually leads to the enhancement of IEF.[17-20]

As organic semiconductors have received increasing attention in the field of photocatalysis, understanding the source and enhancement strategies of their IEF has become a critical task.[21-25] Since the organic compounds can adjust the structure by adding substituent groups, and the electronegativity of the substituent groups has an important influence on the electron distribution and molecular dipole of organic molecular photocatalysts, the molecular dipole and IEF can be effectively enhanced by selecting appropriate substituents and improving the crystallinity and uniformity of organic semiconductors.[26-29] As an organic semiconductor material, g-C_3N_4 is mainly composed of light elements such as C, N, and H, and has a van der Waals layered structure. It has been widely used in photocatalysis, electrocatalysis, and other fields in recent years.[30-34] However, g-C_3N_4 prepared by traditional thermal condensation and other methods has the shortcomings such as low crystallinity and fast photogenerated carrier recombination. Therefore, various modifications are often performed on g-C_3N_4, including morphology control, enhancement of crystallinity, modulation of electronic structure by heteroatom doping, etc.[35-38] Among them, doping heteroatoms into the lattice of g-C_3N_4 is not only an effective way to improve visible light absorption, but also can significantly enhance the IEF strength and realize the spatial separation of photogenerated electron-hole pairs.[39-41]

The optimization and modification of catalysts by doping with different elements is a common method[41]. The activity of g-C_3N_4 can be improved by introducing non-metal elements such as O, P, S, etc.[42-47] Yang et al.[48] formed an IEF in g-C_3N_4 nanosheets by co-doping O and N, which significantly enhances the lifetime of photogenerated carriers and inhibits the recombination of them.

DOI: 10.14102/j.cnki.0254-5861.2022-0103

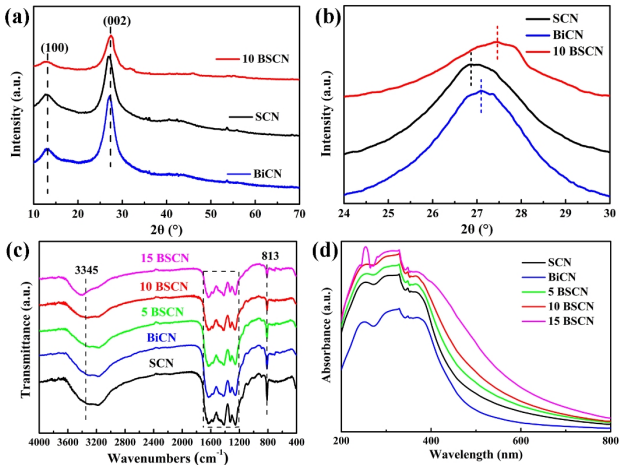

Figure 1. XRD patterns of as-prepared samples (a); Partially enlarged view (2 Theta at 24°-30°) (b); FTIR (c) and UV-Vis DRS (d) spectra of as-prepared samples.

In addition, there are also works on optimizing the electronic structure and photocatalytic performance of g-C_3N_4 by doping metal elements such as Co, Cu, Ni, and so on.[49-51] For example, Ye et al.[52] successfully fabricated a highly dispersed Co, O co-doped porous g-C_3N_4 heterostructure (Co-O@CN), which can completely degrade ofloxacin within 20 min. Among them, the synergistic effect of Co and O realizes the reconfiguration of the intrinsic electronic structure of g-C_3N_4 and effectively improves the stability of the catalyst.

In order to enhance the IEF of g-C_3N_4 and improve the carrier dynamics, Bi and S co-doped g-C_3N_4 photocatalyst with strong visible light absorption and high carrier separation efficiency was synthesized by a two-step heating method. By doping with non-metallic S and Bi elements, the electronic structure of g-C_3N_4 is modified and improved, and the performances of photocatalytic degradation and H_2 production are significantly improved. It first quantitatively characterizes the strength of IEF in the experimental analysis of co-doped g-C_3N_4, which provides an important reference for that element co-doping can control the IEF of g-C_3N_4-based photocatalysts. In addition, this study provides a deeper understanding of the catalytic mechanism of g-C_3N_4-based photocatalysts and its structure-activity relationship for the efficient utilization of solar energy for photocatalytic degradation and H_2 production.

n RESULTS AND DISCUSSION

Structure and Morphology Characterization. The crystal structures and phases of the prepared SCN, BiCN and 10 BSCN samples were analyzed by XRD. The XRD peaks of g-C_3N_4 at 13.1° and 27.5° are attributed to its (100) and (002) planes, compared to the JCPDS card (PDF#87-1526).[53] Figure 1a shows two distinct peaks of SCN, of which the peak at 12.9° is attributed to the (100) plane formed by the packing of 3-s-triazine units in a planar structure, and the strong one at 26.9° is caused by the (002) crystal plane of SCN, corresponding to the interlayer stacking of C-N conjugated aromatic heterocycles, which proves that the doped sample still maintains the basic structure of g-C_3N_4. The XRD characteristic peak of SCN is blue-shifted relative to the standard peak of g-C_3N_4, which indicates that the interlayer spacing of SCN prepared by the two-step heating method increases compared with that of g-C_3N_4, which may be caused by the doping of S atoms.[54] As the atomic radius of S is larger than that of C and N, the lattice distortion of g-C_3N_4 crystals occurs after doping with S atoms. In contrast, the XRD peak of BiCN is located at 27.1°, which is weaker than the blue shift of SCN due to the less doping of Bi element, resulting in less lattice distortion of BiCN. Figure 1b is a partially enlarged view of Figure 1a. In the XRD pattern of 10 BSCN, the high-intensity diffraction peak appears around 27.5°, indicating that the (002) crystal plane of BSCN sample slightly shifts to a high angle after calcination and reflux operation. This may be due to the adsorption of BSCN sample during the reflow process, which increases the stacking degree of aromatic heterocycles, reduces the distance between nanosheets, and promotes the charge transport between the interfaces.[55] According to the conjugation length of triazine repeating structure, the (100) plane intensity of the reflowed sample decreases, indicating that the crystal plane changes from a long-range conjugated structure to a short-range conjugation. In addition, due to the high dispersibility and low contents of Bi and S elements, no peak of Bi, S, and Bi_2S_3 was found.[56]

To further determine the structure of the prepared samples, FTIR analysis was performed on SCN, BiCN and X BSCN. As shown in Figure 1c, the FTIR spectra proved that the elemental doping of Bi and S did not damage the basic structure of g-C_3N_4. Among them, the peak at 813 cm^{-1} is attributed to the bending vibration of the triazine ring, the 1100-1750 cm^{-1} region corresponds to the typical heterocyclic stretching vibration of g-C_3N_4, and the absorption peak is a broadband near 3345 cm^{-1} corresponds to the residual N-H, N-H_2 in the sample and the adsorption of water molecules in the air.[57] The absorption peaks at 813 and 3345 cm^{-1} in X BSCN gradually weaken with the increase of Bi doping content, and the peak at 813 cm^{-1} becomes sharper. This is precisely due to that the incorporation of Bi and S into the lattice of g-C_3N_4 increases the bonding ability of X BSCN and improves the stability of the catalyst.[58] In addition, no other impurity peaks

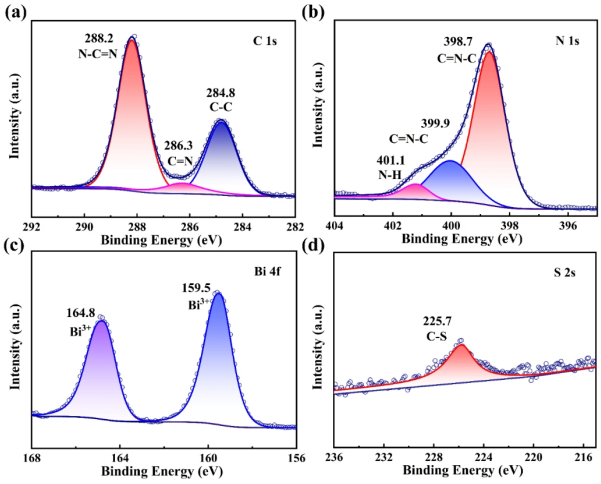

Figure 2. XPS survey spectra of C 1s (a), N 1s (b), Bi 4f (c) and S 2s (d) of sample 10 BSCN.

DOI: 10.14102/j.cnki.0254-5861.2022-0103

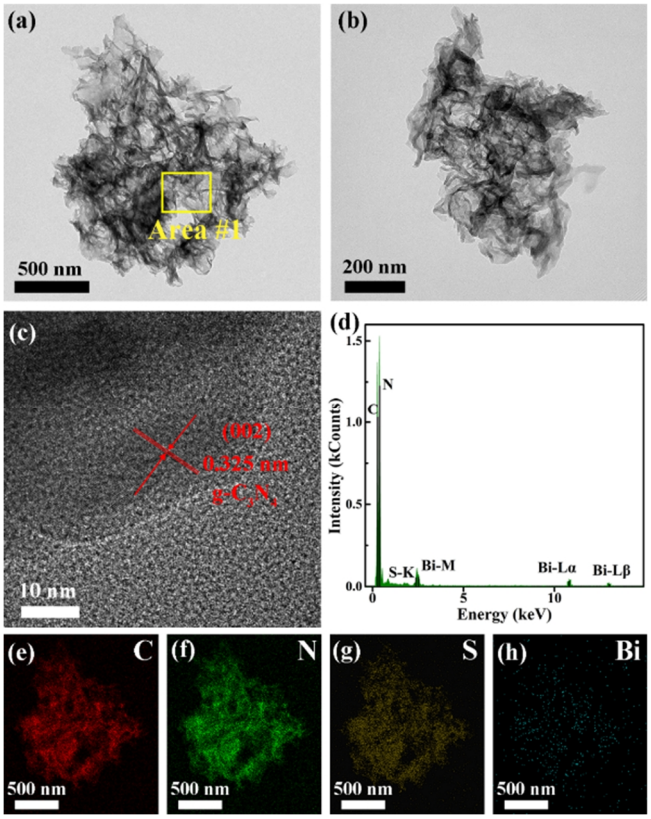

Figure 3. TEM (a-b), HRTEM (c) and EDS (d) of 10 BSCN; Elemental mapping of C, N, S and Bi (e-h).

were found in all samples, indicating that the samples are of high purity. Figure 1d is the UV-Vis DRS map of SCN, BiCN and X BSCN. With the increase of Bi content, the red-shift of the absorption edge of X BSCN is obviously enhanced because the lattice distortion will occur after Bi and S are successfully doped into g-C_3N_4, which can effectively improve the response range of spectrum.

The element species and valence states of 10 BSCN were analyzed by XPS.[59] Figure 2a is the C 1s spectrum, in which the peaks of binding energy at 284.8, 286.1, and 288.0 eV correspond to the C-C, C=N and N-C=N bonds, respectively. Figure 2b is the N 1s spectrum, in which the characteristic peaks at 398.6, 399.8, and 401.1 eV are attributed to C=N-C, N-$(C)_3$ and N-H bonds. Figure 2c is the XPS spectrum of Bi 4f, the binding energy is 158.9 eV, and the characteristic peaks at 164.2 eV correspond to Bi $4f_{7/2}$ and Bi $4f_{5/2}$, indicating that Bi exists mainly in a trivalent state. As shown in Figure 2d, the S 2s orbital can be fitted as a characteristic peak with lower energy at 225.7 eV, corresponding to the C-S bond. According to XPS analysis, the doped Bi and S elements mainly exist in the form of Bi^{3+} ions and C-S bonds, respectively, further indicating that the doping of Bi and S elements.

The morphology and structure of 10 BSCN were characterized by TEM, and the elemental mapping was analyzed by EDS. It can be seen from Figure 3a that the prepared BSCN photocatalyst exhibits a porous 2D nanosheet structure with good dispersibility, indicating that the 2D sheet structure of the original g-C_3N_4 is not changed after Bi and S doping. As shown in Figure 3b, the layer-by-layer structure of the samples can be observed, which means that BSCN has a higher specific surface area, which is very beneficial to improve the light absorption capacity and pollutant adsorption performance. It can be seen from the HRTEM images of Figure 3c that the lattice fringe of 10 BSCN is about 0.325 nm, corresponding to the (002) crystal plane. This indicates that BSCN retains fine crystalline properties, which helps to enhance the IEF and improve the transport efficiency of photogenerated carriers. In particular, the element content was detected for the Area #1 microscopic selection (Figure 3a), and the corresponding spectrum was obtained (Figure 3d). In addition, EDS elemental spectra were collected (Figure 3e-h), which shows that the composites contain a large amount of C and N elements and trace amounts of Bi and S elements, which indicates the successful preparation of BSCN composites.

Photocatalytic Performance. The photocatalytic degradation experiments of TC and BPA were carried out. As shown in Figure 4a, the TC photodegradation activity of co-doped X BSCN photocatalyst is significantly higher than that of single-doped SCN and BiCN. Among them, 10 BSCN has the highest photodegradation rate of TC, indicating that appropriate amount of Bi and S co-doping can significantly improve the photocatalytic degradation of TC. In addition, kinetic equations were obtained by linear fitting transformation (Figure 4b), where *k* is the apparent rate constant for the degradation of TC by the photocatalyst.[60] After 60 min of irradiation, the apparent rate of photodegradation for TC by sample

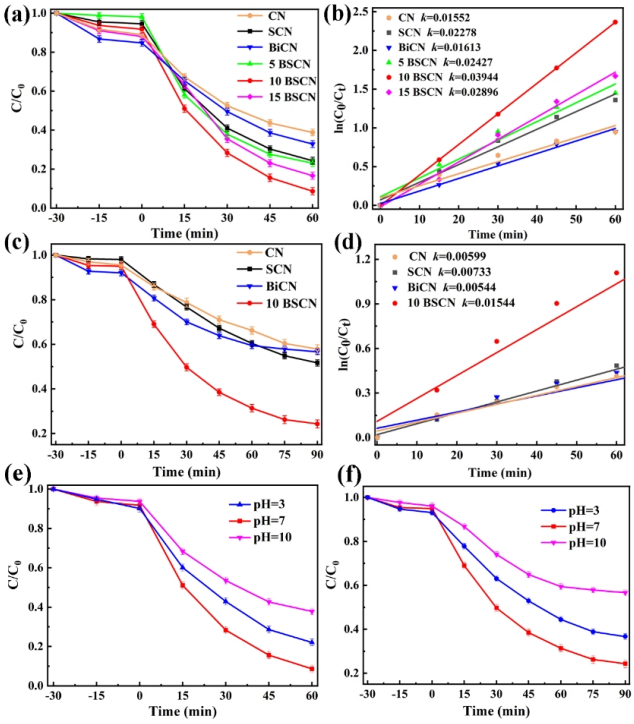

Figure 4. Photocatalytic degradation efficiency of TC (a) and apparent rate constant of linear fitting (b); Photocatalytic degradation efficiency of BPA (c) and apparent rate constant of linear fitting (d); The effects of initial pH value on the photocatalytic degradation of TC (e) and BPA (f).

DOI: 10.14102/j.cnki.0254-5861.2022-0103

Table 1. HER of the As-prepared Samples with Other Published Similar Catalysts

Catalyst sample	Light source (λ > 420 nm)	Sacrificial agent	H_2 production rate (μmol·g^{-1}·h^{-1})	Ref.
10 BSCN	300 W Xe lamp	methanol	1139	This work
$LaCoO_3$/g-C_3N_4	35 W HID Xe lamp	methanol	200	[37]
Co-La/g-C_3N_4	35 W UV-Vis Xe lamp	methanol	250	[50]
3Ru-Ti_3AlC_2/g-C_3N_4	300 W Xe lamp	methanol	1445	[61]
Ni_3C@Ni/g-C_3N_4	350 W Xe lamp	TEOA	1120	[62]
$Cu(OH)_2$/g-C_3N_4	150 W Xe lamp	TEOA	187	[63]
SS-CN	300 W Xe lamp	TEOA	982.33	[64]

10 BSCN reaches 0.03944 min^{-1}, which is 1.73 times that of SCN and 2.45 times that of BiCN, respectively. In addition, as shown in Figure 4c, after 90 min of visible light irradiation, the photodegradation rate of 10 BSCN to BPA reaches 75.7%, and its photocatalytic degradation activity is significantly improved compared with SCN and BiCN. It can be seen from Figure 4d that sample 10 BSCN has the largest *k* value, which is 0.01544 min^{-1}. In addition, the effect of the pH of reaction solution on the photocatalytic performance was also investigated. As shown in Figure 4e-f, sample 10 BSCN exhibits remarkable photocatalytic degradation activity under neutral conditions. According to the above experiments, the proper introduction of Bi and S can improve the ability of photocatalytic degradation of organic pollutants.

The photocatalytic performance of the prepared samples was also evaluated by water splitting experiments for H_2 production. As shown in Figure 5a, the 10 BSCN sample with better degradation activity also exhibits significant photocatalytic H_2 evolution activity under visible light irradiation. Its H_2 evolution efficiency is 1139 μmol·g^{-1}·h^{-1}, which is 2.5, 1.8 and 2.4 times that of CN, SCN and BiCN. This may be mainly attributed to the introduction of Bi and S, promoting the adsorption of hydrogen species on the g-C_3N_4 nanosheets, which in turn exhibits excellent HER activity. To illustrate the stability of the 10 BSCN photocatalyst, the photocatalytic performances of SCN, BiCN, and 10 BSCN were all performed in triplicate (Figure 5b). Among them, 10 BSCN still shows stable HER activity, indicating that Bi and S co-doping can effectively improve the photocatalytic activity.

The H_2 production performance of X BSCN photocatalyst was compared with that of other published similar g-C_3N_4-based materials, as shown in Table 1. The H_2 evolution efficiency of 10 BSCN also reaches a high level. Furthermore, an excellent photocatalyst should have not only broad spectrum but also good stability. To this end, cycling experiments for the degradation of TC were carried out on 10 BSCN. As shown in Figure 6a, after three cycles, the photocatalytic degradation efficiency of TC by 10 BSCN decreases slightly, which may be caused by the loss of the sample during separation and recovery. Nonetheless, after three cycles, the photocatalytic degradation efficiency of TC by 10 BSCN still reaches 89.4%. Subsequently, the XRD, FTIR and UV-Vis DRS of the 10 BSCN samples before and after the cycling stability test were examined (Figure 6b-d), showing the cyclic photocatalysis experiment has little effect on the crystal structure, functional group structure and light response range of the photocatalyst. In other words, the 10 BSCN sample synthesized by reflux self-assembly maintains quite excellent photocatalytic performance and structural stability during the photocatalytic process.

Analysis of the Photocatalytic Mechanism. Under visible light irradiation, related photoelectrochemical experiments were carried out on SCN, BiCN and X BSCN, and the effects of Bi and S co-doping on the activity of g-C_3N_4 photocatalyst are further discussed from the perspective of carrier separation and charge transport. Generally, photocatalysts with high separation rate and high mobility will transport more electrons and holes to the surface of the material, so that the carbon sheet electrode loaded with this photocatalyst can detect a larger photocurrent.[65,66] As shown in

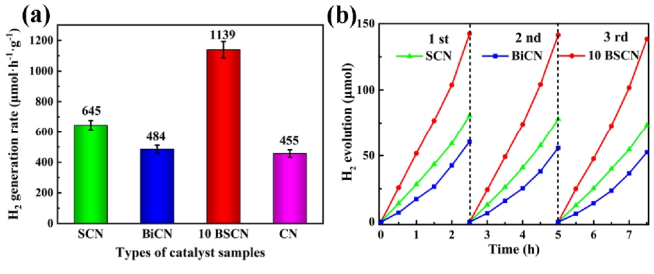

Figure 5. H_2 production rate of different photocatalysts under visible light irradiation (a); Cycle curve of hydrogen evolution of SCN, BiCN and 10 BSCN (b).

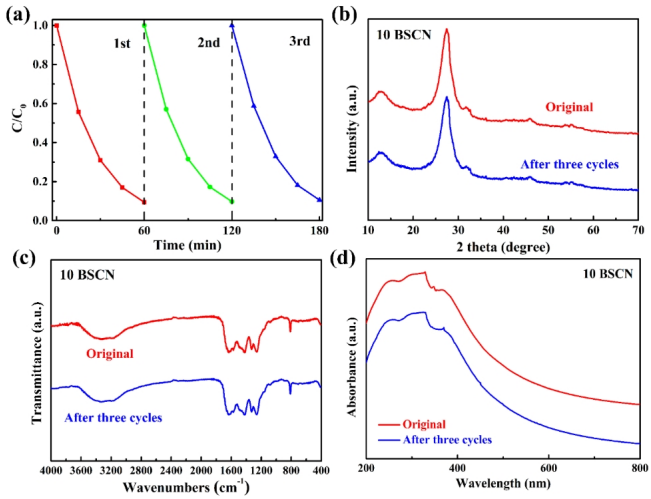

Figure 6. Cycle experiment of photodegradation for TC by sample 10 BSCN (a), XRD (b), FTIR (c) and UV-Vis DRS (d) of 10 BSCN photocatalyst before and after the cycle stability experiment.

DOI: 10.14102/j.cnki.0254-5861.2022-0103

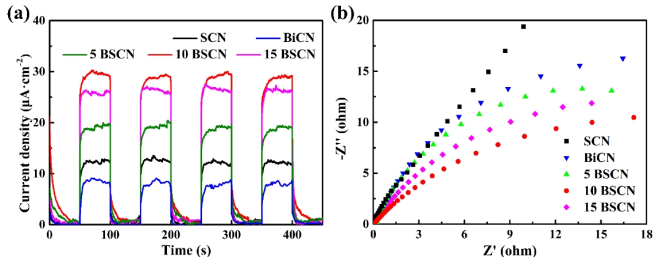

Figure 7. Transient photocurrent curves (a) and EIS (b) of SCN, BiCN and X BSCN.

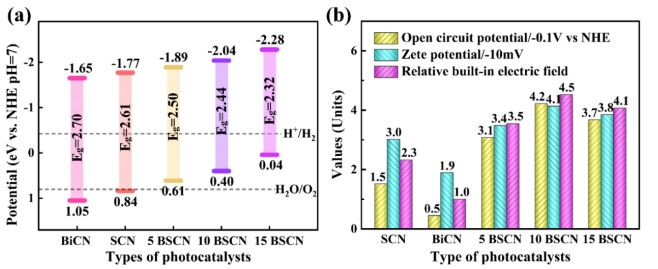

Figure 9. Energy band structure of the prepared samples (a) and strength of IEF in all samples (b).

Figure 7a, the curves appear jitter after light irradiation, which can be attributed to the interference of background light and the rotation of the rotor. The photocurrents of BiCN and SCN under visible light irradiation are relatively small, while that of X BSCN shows a trend of first increasing and then decreasing with the increase of doping amount, which proves that the charge separation within or on the surface of the catalyst is more rapid. Similar results can also be obtained from EIS (Figure 7b). In EIS curve, the smaller the radius of the arc, the smaller the corresponding charge transfer resistance of the material. 10 BSCN shows the largest photocurrent and the smallest charge transfer resistance because Bi and S effectively enhance the strength of the IEF, which in turn enables the catalyst to obtain faster carrier separation and migration rates.

In addition, the energy band position of X BSCN can be determined by Mott-Schottky (MS) curve and Tauc plot curve. Figure 8a-e show the measured flat-band potential values of SCN, BiCN and X BSCN at frequencies of 0.5, 1.0 and 1.5 kHz, respectively. After conversion, the E_{FB} of SCN, BiCN and X BSCN are about -1.77, -1.65, -1.89, -2.04, and -2.28 V, respectively (vs. NHE, pH = 7). In addition, the straight lines of the measured MS curves have positive slopes, indicating that they are all n-type semiconductors. Generally, the bottom value of the conduction band of n-type semiconductors is approximately equal to the flat band potential, so it is approximately considered that the potential values of the lowest molecularly unoccupied orbital (LUMO) of the prepared samples, E_{LUMO}, are -1.77, -1.65, -1.89, -2.04 and -2.28 eV, respectively.

Figure 8f is a Tauc plot transformed based on the UV-Vis DRS curve of Figure 1d. The band gap values (E_g) of SCN, BiCN, 5 BSCN, 10 BSCN and 15 BSCN are 2.61, 2.70, 2.50, 2.44 and 2.32 eV, respectively. Then, the potential values of the highest molecularly occupied orbital (E_{HOMO}) of each sample can be calculated to be 0.84, 1.05, 0.61, 0.40 and 0.04 eV, respectively.

Figure 9a is the energy band structure diagram of the prepared samples SCN, BiCN and X BSCN after summarizing. It can be seen that different Bi and S doping has a great influence on the band gap structure of the g-C_3N_4 photocatalytic material. Among them, BiCN has a wider band gap due to less doping; the band gap of SCN is relatively narrow, and the LUMO orbital position also moves up accordingly; while with the increase of Bi doping amount, the band gap of X BSCN gradually narrows, and the conduction band position also moves up, resulting in a strong reduction ability. However, with the narrowing of the band gap, the recombination rate of photogenerated electron holes increases, which may lead to the weakening of the degradation performance. Previous studies on photocatalytic degradation activity also proved that appropriate amount of Bi and S doping can greatly improve the photocatalytic performance. In order to explore the relationship between Bi/S co-doping and IEF, the Kanata model is used to perform related experimental characterization and calculation of the IEF intensity of the prepared samples based on the IEF characterization method proposed by Zhu et al.[27]. The Kanata model demonstrates that the strength of IEF is determined by the surface potential and surface charge density.

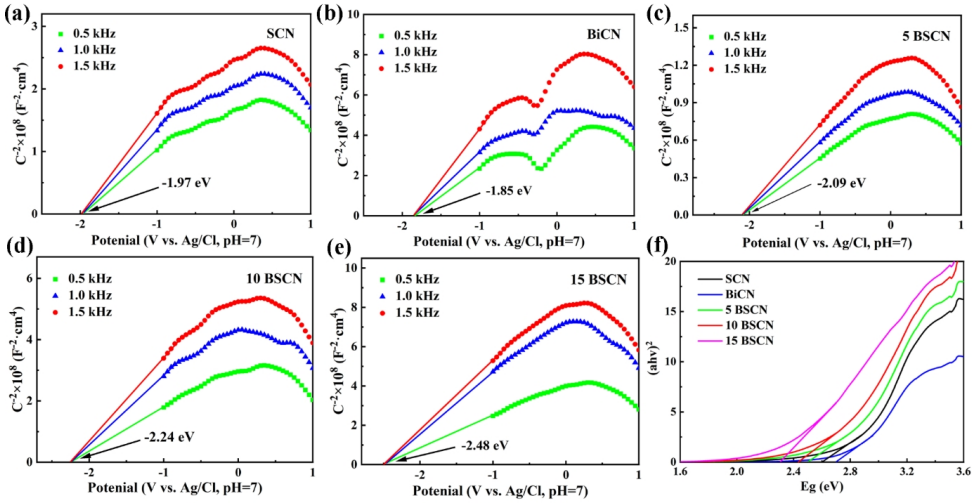

Figure 8. MS curves of SCN (a), BiCN (b), 5 BSCN (c), 10 BSCN (d) and 15 BSCN (e); Tauc plots of prepared samples (f).

DOI: 10.14102/j.cnki.0254-5861.2022-0103

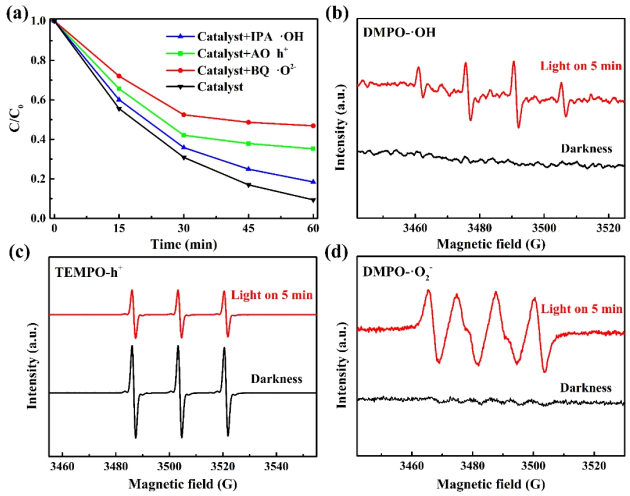

Figure 10. Free capture curves of 10 BSCN in TC degradation experiment (a); ESR detection of 10 BSCN under dark and visible light irradiation (b-d).

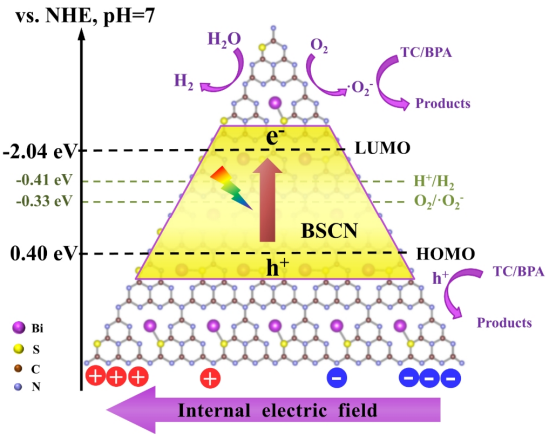

Figure 11. Photocatalytic mechanism of the Bi and S co-doped g-C_3N_4.

$$F_s = (-2V_s\rho/\varepsilon\varepsilon_0)^{1/2} \quad (1)$$

Where F_s is the IEF amplitude, V_s is the surface potential, ρ is the surface charge density, ε is the low-frequency permittivity, and ε_0 is the vacuum permittivity. It can be seen from the above formula that the size of IEF is mainly determined by the surface potential V_s and the surface charge density ρ. The surface potential V_s can be characterized by the open circuit potential, and the surface charge density ρ can be determined by the Zeta potential. Figure 9b shows the open circuit potential (vs. NHE) and Zeta potential values of each photocatalyst, and the resulting relative IEF intensity values are then estimated by substituting into Formula (1). The IEF intensity of BiCN is normalized to 1.0, and the relative values of IEF intensity of SCN, 5 BSCN, 10 BSCN and 15 BSCN are 2.3, 3.5, 4.5 and 4.1, respectively. Combining with the above degradation effects, it can be further inferred that Bi/S co-doping can effectively tune the IEF intensity, thus endowing 10 BSCN with a strong IEF, which enhances the photocatalytic activity by promoting the generation and separation of the photogenerated carriers.

Figure 10a is the radical capture experiment performed with 10 BSCN as the photocatalyst and TC as the target pollutant. After 60 min of visible light irradiation, the photocatalytic degradation efficiency of TC by 10 BSCN in the blank group reaches 90.6%, while the degradation efficiency of TC in the experimental group added with IPA, AO or *p*-BQ before the reaction is only 81.6%, 64.8% and 53.1%, respectively. The photocatalytic performance of the experimental group is significantly inhibited. Among them, the experimental group with IPA added has little effect on the removal of TC. The reason is that the redox potential E_{HOMO} corresponding to the HOMO of the 10 BSCN photocatalyst is smaller than that of $E_{OH\text{-}/\cdot OH}$ (2.29 V vs. NHE), which makes it difficult to generate ·OH. In addition, the ESR detection results also confirm the existence of ·OH, h^+ and $\cdot O_2^-$ radicals in the 10 BSCN photocatalyst. As shown in Figure 10b-d, no ·OH and $\cdot O_2^-$ signals are observed under dark conditions. However, the signal intensities of them increase significantly after light irradiation. The signal of h^+ decreases significantly after irradiation, which indicates that part of h^+ can participate in the photocatalytic reaction, so as to enhance the ·OH signal.

Based on the above results and discussions, a possible photocatalytic reaction mechanism of 10 BSCN is proposed (Figure 11). First, the unique porous ultra-thin sheet structure of g-C_3N_4 endows the catalyst with considerable advantages in photo redox reactions, such as more exposed surface-active sites, shortening the migration distance from bulk to surface, and promoting transfer of reactants and products. Secondly, the doping of appropriate amount of Bi and S can greatly improve the in-plane mobility of photogenerated carriers along the in-plane direction. At the same time, the higher IEF enables more electrons and holes to be separated and provides a stronger driving force for their transfer from the bulk to the surface. In addition, a more negative conduction band potential can make the photogenerated electrons have a higher kinetic overpotential, which in turn promotes the efficient generation of the photogenerated electrons, and finally achieves the purpose of degrading organic contaminants and water splitting.

n CONCLUSION

In conclusion, a template-free self-assembled Bi and S co-doped g-C_3N_4 sample was successfully synthesized by two-step elevated temperature calcination and solvothermal reflux method, and the sample showed robust catalytic activity and stability in the degradation of TC, BPA, and the water splitting reaction for hydrogen evolution. Among all the synthesized samples, 10 BSCN exhibited the best photocatalytic degradation and hydrogen evolution rates. That is, under visible light irradiation, the TC degradation rate constant is 0.03944 min^{-1}, and the HER rate is 1139 $\mu mol \cdot g^{-1} \cdot h^{-1}$. This dramatic improvement in catalytic performance is attributed to the widening of the light response range, the maximal utilization of reactive sites, and the synergistic advantage of providing a strong internal driving force for the separation and rapid migration of photogenerated carriers. In addition, this work also provides a novel solution for the construction of highly active, stable, and inexpensive g-C_3N_4-based materials by heteroatom doping, which can be expected to be widely used in photocatalysis, photoelectrocatalysis, and other related fields.

DOI: 10.14102/j.cnki.0254-5861.2022-0103

n EXPERIMENTAL

Experimental Reagents

Experimental Reagents. Urea (Shantou Xilong Scientific Co. Ltd., Shantou, China), thioacetamide (Tianjin Kemio Chemical Reagent Co. Ltd., Tianjin, China), bismuth nitrate pentahydrate (Shanghai Macklin Biochemical Co., Ltd.), glycerol (Shantou Xilong Scientific Co. Ltd., Shantou, China), ethanol (Shantou Xilong Scientific Co. Ltd., Shantou, China). All reagents were analytically pure and used without further purification.

Preparation of the Samples. The preparation of S doped g-C_3N_4 (SCN) was performed according to the published paper.[67] In the preparation process of Bi and S co-doped g-C_3N_4, a certain amount of $Bi(NO_3)_3 \cdot 5H_2O$ and 15 g urea were added to 20 mL of deionized water, which was magnetically stirred at 50 °C for 0.5 h. 100 mg of TAA was added to continue stirring for 0.5 h until the solution turned amber and then the same calcination procedure was done as SCN. After cooling to room temperature, it was ground, sieved, and thoroughly washed with water and ethanol, then the Bi and S co-doped g-C_3N_4 yellow powder was obtained after drying. The obtained products were named X BSCN, where X represents the different addition amounts of Bi sources, which are 5, 10, and 15 mg, respectively. For comparison, Bi doped g-C_3N_4 (BiCN) powder was prepared under similar conditions by adding 10 mg of Bi source and 15 g of urea to 20 mL of deionized water.

Characterization

The phase composition of photocatalysts was characterized by Bruker D8 Advance X-ray diffraction (XRD) with Cu Kα (λ = 0.1541 nm) radiation. The microstructures and mapping were observed by the FEI Talos F200X transmission electron microscopy (TEM) with energy dispersive X-ray spectrometer (EDS). The infrared spectra including the structural composition and chemical functional groups of the samples were obtained by Nicolet NEXUS 670 spectrometer (Thermo Co. Ltd., Madison, WI, USA). The chemical states were analyzed by the Shimadzu Axis Ultra DLD X-ray photoelectron spectroscopy (XPS) with Al Kα radiation. The ultraviolet visible diffuse reflectance spectroscopy (UV-Vis-DRS) was detected by the Shanghai Metash UV-9000 ultraviolet visible spectrophotometer equipped with an integrating sphere. Electrochemical analyzer with three-electrode system (Chenhua CHI760E, Shanghai, China) was employed to analyze the photoelectrochemical properties. In addition, Ag/AgCl electrode, Pt sheet (20 × 20 × 0.1 mm^3), and carbon paper coated with photocatalyst (1 × 1.5 cm^2, HCP030 N, Shanghai Hesen, China) were used as the reference electrode, counter electrode and working electrode, respectively. A 300 W xenon lamp (PLS-SXE 300, Beijing Perfect Light, Beijing, China) was used as visible light source and 0.5 mol·L^{-1} Na_2SO_4 solution as electrolyte. Open circuit potential time curve (OCPT), electrochemical impedance spectroscopy (EIS), Mott Schottky (MS) and photocurrent response curve were measured on an electrochemical analyzer. Electron spin resonance (ESR) spectra were recorded on a JEOL FA-200 spectrometer. Zeta potential was measured on a ZetaProbe (Collidal dynamics Co. Ltd., USA).

Photocatalytic Performance Test

Photocatalytic Degradation of Tetracycline (TC) and Bisphenol A (BPA). The photocatalytic degradation of TC (50 mg·L^{-1}) and BPA (20 mg·L^{-1}) was studied in a quartz reactor under visible light. First, 50 mL of prepared TC or BPA solution was added, followed by adding 50 mg of photocatalyst, and then the mixed solution was stirred in dark for 0.5 h to achieve physical dynamic adsorption equilibrium. Finally, the photocatalytic degradation experiment of TC or BPA was carried out under the 300 W Xenon lamp.

Photocatalytic H_2 Production. First, 50 mg of the sample was added to 90 mL of deionized water, and 10 mL of methanol was added as a sacrificial agent. Then, N_2 was passed into the sealing system for 1 h to ensure an anaerobic environment during the photocatalytic water splitting process. A 300 W Xenon lamp (MC-PF300, Beijing Merry Change Technology Co., Ltd) was used as the light source. After 30 min of light irradiation, H_2 was collected and analyzed by an automatic on-line vacuum photocatalytic system (MC-SPB10, Beijing Merry Change Technology Co., Ltd) and a gas chromatograph (GC9720II, Zhejiang Fuli Analytical Instruments Co., Ltd). High-purity N_2 was selected as carrier gas. The samples were taken every 0.5 h to detect the concentration of H_2 in the gas, and high-purity N_2 was bubbled every 2.5 h for 1 h to conduct the photocatalytic H_2 production cycle test.

Photocatalytic Active Group Capture Experiment. *P*-benzoquinone (*p*-BQ, 0.1 mmol·L^{-1}), ammonium oxalate (AO, 10 mmol·L^{-1}) and isopropanol (IPA, 10 mmol·L^{-1}) were used as trapping agents for $\cdot O_2^-$, h^+, and ·OH, respectively. The effects of active intermediates during photodegradation on the performance of photocatalysts were investigated.

n ACKNOWLEDGEMENTS

The authors acknowledge the financial support from the National Natural Science Foundation of China (No. 51962023, 51862024), the Natural Science Foundation of Jiangxi Province, China (No. 20212BAB204045, 20192ACBL21047), the Key Laboratory of Jiangxi Province for Persistent Pollutants Control and Resources Recycle (Nanchang Hangkong University) (No. ES202002077).

n AUTHOR INFORMATION

Corresponding authors. Emails: lixibao@nchu.edu.cn (Xibao Li), dengfang40030@126.com (Fang Deng) and hanlu@ustl.edu.cn (Lu Han)

n COMPETING INTERESTS

The authors declare no competing interests.

n ADDITIONAL INFORMATION

Full paper can be accessed via
http://manu30.magtech.com.cn/jghx/EN/10.14102/j.cnki.0254-5861.2022-0103
For submission: https://mc03.manuscriptcentral.com/cjsc

n REFERENCES

DOI: 10.14102/j.cnki.0254-5861.2022-0103

(1) Jing, J. F.; Yang, J.; Zhang, Z. J.; Zhu, Y. F. Supramolecular zinc porphyrin photocatalyst with strong reduction ability and robust built-in electric field for highly efficient hydrogen production. *Adv. Energy Mater.* **2021**, 11, 2101392.

(2) Yan, T.; Zhang, X. J.; Liu, H.; Jin, Z. L. CeO_2 Particles anchored to Ni_2P nanoplate for efficient photo-catalytic hydrogen evolution. *Chin. J. Struct. Chem.* **2022**, 41, 2201047-2201053.

(3) Li, J.; Cai, L. J.; Shang, J.; Yu, Y.; Zhang, L. Z. Giant enhancement of internal electric field boosting bulk charge separation for photocatalysis. *Adv. Mater.* **2016**, 28, 4059-4064.

(4) Liu, Y.; Yu, F. B.; Wang, F.; Bai, S. J.; He, G. W. Construction of Z-scheme In_2S_3-TiO_2 for CO_2 reduction under concentrated natural sunlight. *Chin. J. Struct. Chem.* **2022**, 41, 2201034-2201039.

(5) Li, X. B.; Wang, W. W.; Dong, F.; Zhang, Z. Q.; Han, L.; Luo, X. D.; Huang, J. T.; Feng, Z. J.; Chen, Z.; Jia, G. H.; Zhang, T. R. Recent advances in noncontact external-field-assisted photocatalysis: from fundamentals to applications. *ACS Catal.* **2021**, 11, 4739-4769.

(6) Guo, L.; Chen, Y.; Ren, Z.; Li, X.; Zhang, Q.; Wu, J.; Li, Y.; Liu, W.; Li, P.; Fu, Y.; Ma, J. Morphology engineering of type-II heterojunction nanoarrays for improved sonophotocatalytic capability. *Ultrason. Sonochem.* **2021**, 81, 105849.

(7) Dai, B. Y.; Fang, J. J.; Yu, Y. R.; Sun, M. L.; Huang, H. M.; Lu, C. H.; Kou, J. H.; Zhao, Y. J.; Xu, Z. Z. Construction of infrared-light-responsive photoinduced carriers driver for enhanced photocatalytic hydrogen evolution. *Adv. Mater.* **2020**, 32, 1906316.

(8) Guo, Y.; Shi, W. X.; Zhu, Y. F.; Xu, Y. P.; Cui, F. Y. Enhanced photoactivity and oxidizing ability simultaneously via internal electric field and valence band position by crystal structure of bismuth oxyiodide. *Appl. Catal. B-Environ.* **2020**, 262, 118262.

(9) Fu, Y. M.; Ren, Z. Q.; Wu, J. Z.; Li, Y. Q.; Liu, W. L.; Li, P.; Xing, L. L.; Ma, J.; Wang, H.; Xue, X. Y. Direct Z-scheme heterojunction of ZnO/MoS_2 nanoarrays realized by flowing-induced piezoelectric field for enhanced sunlight photocatalytic performances. *Appl. Catal. B-Environ.* **2021**, 285, 119785.

(10) Wang, Z. L.; Cheng, B.; Zhang, L. Y.; Yu, J. G.; Tan, H. Y. BiOBr/NiO S-scheme heterojunction photocatalyst for CO_2 photoreduction. *Sol. RRL*. **2022**, 6, 2100587.

(11) Zhang, H. M.; Li, D. F.; Byun, W. J.; Wang, X. L.; Shin, T. J.; Jeong, H. Y.; Han, H. X.; Li, C.; Lee, J. S. Gradient tantalum-doped hematite homojunction photoanode improves both photocurrents and turn-on voltage for solar water splitting. *Nat. Commun.* **2020**, 11, 4622.

(12) Zhang, L. Y.; Zhang, J. J.; Yu, H. G.; Yu, J. G. Emerging S-scheme photocatalyst. *Adv. Mater.* **2022**, 34, 2107668.

(13) Wang, X. H.; Huang, J. F.; Li, S. X.; Meng, A.; Li, Z. J. Interfacial chemical bond and internal electric field modulated Z-scheme S-v-$ZnIn_2S_4$/$MoSe_2$ photocatalyst for efficient hydrogen evolution. *Nat. Commun.* **2021**, 12, 4112.

(14) Dong, S. Y.; Cui, L. F.; Tian, Y. J.; Xia, L. J.; Wu, Y. H.; Yu, J. J.; Bagley, D. M.; Sun, J. H.; Fan, M. H. A novel and high-performance double Z-scheme photocatalyst ZnO-SnO_2-Zn_2SnO_4 for effective removal of the biological toxicity of antibiotics. *J. Hazard. Mater.* **2020**, 399, 123017.

(15) Guo, Y.; Shi, W. X.; Zhu, Y. F. Internal electric field engineering for steering photogenerated charge separation and enhancing photoactivity. *EcoMat.* **2019**, 1, 12007.

(16) Xia, B. H.; Deng, F.; Zhang, S. Q.; Hua, L.; Luo, X. B.; Ao, M. Y. Design and synthesis of robust Z-scheme ZnS-SnS_2 n-n heterojunctions for highly efficient degradation of pharmaceutical pollutants: performance, valence/conduction band offset photocatalytic mechanisms and toxicity evaluation. *J. Hazard. Mater.* **2020**, 392, 122345.

(17) Dong, S. Y.; Xia, L. J.; Chen, X. Y.; Cui, L. F.; Zhu, W.; Lu, Z. S.; Sun, J. H.; Fan, M. H. Interfacial and electronic band structure optimization for the adsorption and visible-light photocatalytic activity of macroscopic $ZnSnO_3$/graphene aerogel. *Compos. Part. B-Eng.* **2021**, 215, 108765.

(18) Wageh, S.; Al-Ghamdi, A. A.; Jafer, R.; Li, X.; Zhang, P. A new heterojunction in photocatalysis: S-scheme heterojunction. *Chin. J. Catal.* **2021**, 42, 667-669.

(19) Wang, W. W.; Li, X. B.; Deng, F.; Liu, J. Y.; Gao, X. M.; Huang, J. T.; Xu, J. L.; Feng, Z. J.; Chen, Z.; Han, L. Novel organic/inorganic PDI-Urea/BiOBr S-scheme heterojunction for improved photocatalytic antibiotic degradation and H_2O_2 production. *Chin. Chem. Lett.* **2022**, 10.1016/j.cclet.2022.01.058.

(20) Xiong, J.; Li, X. B.; Huang, J. T.; Gao, X. M.; Chen, Z.; Liu, J. Y.; Li, H.; Kang, B. B.; Yao, W. Q.; Zhu, Y. F. CN/rGO@BPQDs high-low junctions with stretching spatial charge separation ability for photocatalytic degradation and H_2O_2 production. *Appl. Catal. B-Environ.* **2020**, 266, 118602.

(21) Yang, J.; Jing, J. F.; Zhu, Y. F. A full-spectrum porphyrin-fullerene D-A supramolecular photocatalyst with giant built-in electric field for efficient hydrogen production. *Adv. Mater.* **2021**, 33, 2101026.

(22) Zhu, B. C.; Tan, H. Y.; Fan, J. J.; Cheng, B.; Yu, J. G.; Ho, W. K. Tuning the strength of built-in electric field in 2D/2D g-C_3N_4/SnS_2 and g-C_3N_4/ZrS_2 S-scheme heterojunctions by nonmetal doping. *J. Materiomics* **2021**, 7, 988-997.

(23) Dong, S. Y.; Zhao, Y. L.; Yang, J. Y.; Liu, X. D.; Li, W.; Zhang, L. Y.; Wu, Y. H.; Sun, J. H.; Feng, J. L.; Zhu, Y. F. Visible-light responsive PDI/rGO composite film for the photothermal catalytic degradation of antibiotic wastewater and interfacial water evaporation. *Appl. Catal. B-Environ.* **2021**, 291, 120127.

(24) Xu, Q. L.; Wageh, S.; Al-Ghamdi, A. A.; Li, X. Design principle of S-scheme heterojunction photocatalyst. *J. Mater. Sci. Technol.* **2022**, 124, 171-173.

(25) Wang, H.; Wu, Y.; Feng, M. B.; Tu, W. G.; Xiao, T.; Xiong, T.; Ang, H. X.; Yuan, X. Z.; Chew, J. W. Visible-light-driven removal of tetracycline antibiotics and reclamation of hydrogen energy from natural water matrices and wastewater by polymeric carbon nitride foam. *Water Res.* **2018**, 144, 215-225.

(26) Rahman, M.; Tian, H. N.; Edvinsson, T. Revisiting the limiting factors for overall water-splitting on organic photocatalysts. *Angew. Chem. Int. Ed.* **2020**, 59, 16278-16293.

(27) Zhang, H. J.; Chen, X. J.; Zhang, Z. J.; Yu, K. Y.; Zhu, W.; Zhu, Y. F. Highly-crystalline triazine-PDI polymer with an enhanced built-in electric field for full-spectrum photocatalytic phenol mineralization. *Appl. Catal. B-Environ.* **2021**, 287, 119957.

(28) Wang, P.; Li, H. T.; Cao, Y. J.; Yu, H. G. Carboxyl-functionalized graphene for highly efficient H_2 evolution activity of TiO_2 photocatalyst. *Acta Phys.-Chim. Sin.* **2021**, 37, 2008047.

(29) Liu, M. R.; Lin, Y. P.; Wang, K.; Chen, S. M.; Wang, F.; Zhou, T. H. Hierarchical cobalt phenylphosphonate nanothorn flowers for enhanced electrocatalytic water oxidation at neutral pH. *Chin. J. Catal.* **2020**, 41, 1654-1662.

(30) Wang, H.; Zhang, J. J.; Yuan, X. Z.; Jiang, L. B.; Xia, Q.; Chen, H. Y. Photocatalytic removal of antibiotics from natural water matrices and swine wastewater via Cu(I) coordinately polymeric carbon nitride framework.

DOI: 10.14102/j.cnki.0254-5861.2022-0103

Chem. Eng. J. **2020**, 392, 123638.
(31) Li, X. B.; Xiong, J.; Gao, X. M.; Huang, J. T.; Feng, Z. J.; Chen, Z.; Zhu, Y. F. Recent advances in 3D g-C_3N_4 composite photocatalysts for photocatalytic water splitting, degradation of pollutants and CO_2 reduction. *J. Alloy. Compd.* **2019**, 802, 196-209.
(32) Fu, J. W.; Yu, J. G.; Jiang, C. J.; Cheng, B. g-C_3N_4-based heterostructured photocatalysts. *Adv. Energy Mater.* **2018**, 8, 1701503.
(33) Yan, F. P.; Wu, Y. H.; Jiang, L. Q.; Xue, X. G.; Lv, J. Q.; Lin, L. Y.; Yu, Y. L.; Zhang, J. Y.; Yang, F. G.; Qiu, Y. Design of C_3N_4-based hybrid heterojunctions for enhanced photocatalytic hydrogen production activity. *ChemSusChem.* **2020**, 13, 876-881.
(34) Wang, M.; Cheng, J.; Wang, X.; Hong, X.; Yu, H. G. Sulfur-mediated photodeposition synthesis of NiS cocatalyst for boosting H_2 evolution performance of g-C_3N_4 photocatalyst. *Chin. J. Catal.* **2021**, 42, 37-45.
(35) Liang, Y. J.; Wu, X.; Liu, X. Y.; Li, C. H.; Liu, S. W. Recovering solar fuels from photocatalytic CO_2 reduction over W^{6+}-incorporated crystalline g-C_3N_4 nanorods by synergetic modulation of active centers. *Appl. Catal. B Environ.* **2021**, 304, 120978.
(36) Hasija, V.; Raizada, P.; Sudhaik, A.; Sharma, K.; Kumar, A.; Singh, P.; Jonnalagadda, S. B.; Thakur, V. K. Recent advances in noble metal free doped graphitic carbon nitride based nanohybrids for photocatalysis of organic contaminants in water: a review. *Appl. Mater. Today* **2019**, 15, 494-524.
(37) Tasleem, S.; Tahir, M. Constructing $La_xCo_yO_3$ perovskite anchored 3D g-C_3N_4 hollow tube heterojunction with proficient interface charge separation for stimulating photocatalytic H_2 production. *Energy Fuels* **2021**, 35, 9727-9746.
(38) Ong, W. J.; Putri, L. K.; Tan, Y. C.; Tan, L. L.; Li, N.; Ng, Y. H.; Wen, X. M.; Chai, S. P. Unravelling charge carrier dynamics in protonated g-C_3N_4 interfaced with carbon nanodots as co-catalysts toward enhanced photocatalytic CO_2 reduction: a combined experimental and first-principles DFT study. *Nano Res.* **2017**, 10, 1673-1696.
(39) Zhu, B. C.; Cheng, B.; Zhang, L. Y.; Yu, J. G. Review on DFT calculation of s-triazine-based carbon nitride. *Carbon Energy* **2019**, 1, 32-56.
(40) Zhang, H. X.; Hong, Q. L.; Li, J.; Wang, F.; Huang, X. S.; Chen, S. M.; Tu, W. G.; Yu, D. S.; Xu, R.; Zhou, T. H.; Zhang, J. Isolated square-planar copper center in boron imidazolate nanocages for photocatalytic reduction of CO_2 to CO. *Angew. Chem. Int. Ed.* **2019**, 58, 11752-11756.
(41) Cheng, L.; Yue, X.; Fan, J.; Xiang, Q. Site-specific electron-driving observations of CO_2-to-CH_4 photoreduction on co-doped CeO_2/crystalline carbon nitride S-scheme heterojunctions. *Adv. Mater.* **2022**, 2200929.
(42) Sun, H. R.; Guo, F.; Pan, J. J.; Huang, W.; Wang, K.; Shi, W. L. One-pot thermal polymerization route to prepare N-deficient modified g-C_3N_4 for the degradation of tetracycline by the synergistic effect of photocatalysis and persulfate-based advanced oxidation process. *Chem. Eng. J.* **2021**, 406, 126844.
(43) Uddin, A.; Rauf, A.; Wu, T.; Khan, R.; Yu, Y. L.; Tan, L.; Jiang, F.; Chen, H. In_2O_3/oxygen doped g-C_3N_4 towards photocatalytic BPA degradation: balance of oxygen between metal oxides and doped g-C_3N_4. *J. Colloid Interface Sci.* **2021**, 602, 261-273.
(44) Lin, Q. C.; Li, Z. S.; Lin, T. J.; Li, B. L.; Liao, X. C.; Yu, H. Q.; Yu, C. L. Controlled preparation of P-doped g-C_3N_4 nanosheets for efficient photocatalytic hydrogen production. *Chin. J. Chem. Eng.* **2020**, 28, 2677-2688.
(45) Ge, F. Y.; Huang, S. Q.; Yan, J.; Jing, L. Q.; Chen, F.; Xie, M.; Xu, Y. G.; Xu, H.; Li, H. M. Sulfur promoted n-pi* electron transitions in thiophene-doped g-C_3N_4 for enhanced photocatalytic activity. *Chin. J. Catal.* **2021**, 42, 450-459.
(46) Li, X. B.; Kang, B. B.; Dong, F.; Zhang, Z. Q.; Luo, X. D.; Han, L.; Huang, J. T.; Feng, Z. J.; Chen, Z.; Xu, J. L.; Peng, B. L.; Wang, Z. L. Enhanced photocatalytic degradation and H_2/H_2O_2 production performance of S-pCN/$WO_{2.72}$ S-scheme heterojunction with appropriate surface oxygen vacancies. *Nano Energy* **2021**, 81, 105671.
(47) Zou, J.; Liao, G. D.; Jiang, J. Z.; Xiong, Z. G.; Bai, S. S.; Wang, H. T.; Wu, P. X.; Zhang, P.; Li, X. In-situ construction of sulfur-doped g-C_3N_4/defective g-C_3N_4 iso-type step-scheme heterojunction for boosting photocatalytic H_2 evolution. *Chin. J. Struct. Chem.* **2022**, 41, 2201025-2201033
(48) Yan, B.; Du, C.; Yang, G. W. Constructing built-in electric field in ultrathin graphitic carbon nitride nanosheets by N and O codoping for enhanced photocatalytic hydrogen evolution activity. *Small* **2020**, 16, 1905700.
(49) Lu, H.; Li, X. R.; Li , F.; Xu, X. Q.; Zhao, R.; Xiong, C. Y.; Hu, Q.; Miao, Z. Q.; Tian, M. Construction of single-atom Ag embedded O, K co-doped g-C_3N_4 with enhanced photocatalytic efficiency for tetracycline degradation and Escherichia coli disinfection under visible light. *J. Mol. Liq.* **2022**, 352, 118655.
(50) Tasleem, S.; Tahir, M. Synergistically improved charge separation in bimetallic Co-La modified 3D g-C_3N_4 for enhanced photocatalytic H_2 production under UV-visible light. *Int. J. Hydrogn Energy* **2021**, 46, 20995-21012.
(51) Jin, Z. L.; Li, Y. B.; Hao, X. Q. Ni, Co-based selenide anchored g-C_3N_4 for boosting photocatalytic hydrogen evolution. *Acta Phys.-Chim. Sin.* **2021**, 37, 1912033.
(52) Ye, J.; Yang, D. Y.; Dai, J. D.; Li, C. X.; Yan, Y. S.; Wang, Y. Strongly coupled cobalt/oxygen co-doped porous g-C_3N_4 heterostructure with abundant oxygen vacancies modulated the peroxymonosulfate activation pathway. *Chem. Eng. J.* **2021**, 431, 133972.
(53) Li, X. B.; Liu, J. Y.; Huang, J. T.; He, C. Z.; Feng, Z. J.; Chen, Z.; Wan, L. Y.; Deng, F. All organic S-scheme heterojunction PDI-Ala/S-C_3N_4 photocatalyst with enhanced photocatalytic performance. *Acta Phys.-Chim. Sin.* **2021**, 37, 2010030.
(54) Wang, J.; Wang, G. H.; Cheng, B.; Yu, J. G.; Fan, J. J. Sulfur-doped g-C_3N_4/TiO_2 S-scheme heterojunction photocatalyst for Congo Red photodegradation. *Chin. J. Catal.* **2021**, 42, 56-68.
(55) Wang, J.; Yang, Z.; Yao, W. Q.; Gao, X. X.; Tao, D. P. Defects modified in the exfoliation of g-C_3N_4 nanosheets via a self-assembly process for improved hydrogen evolution performance. *Appl. Catal. B-Environ.* **2018**, 238, 629-637.
(56) Li, H.; Deng, F.; Zheng, Y.; Hua, L.; Qu, C. H.; Luo, X. B. Visible-light-driven Z-scheme rGO/Bi_2S_3-BiOBr heterojunctions with tunable exposed BiOBr (102) facets for efficient synchronous photocatalytic degradation of 2-nitrophenol and Cr(VI) reduction. *Environ. Sci.-Nano.* **2019**, 6, 3670-3683.
(57) Huang, Y. Y.; Jian, Y. P.; Li, L. H.; Li, D.; Fang, Z. Y.; Dong, W. X.; Lu, Y. H.; Luo, B. F.; Chen, R. J.; Yang, Y. C.; Chen, M.; Shi, W. D. A NIR-responsive phytic acid nickel biomimetic complex anchored on carbon nitride for highly efficient solar hydrogen production. *Angew. Chem. Int. Ed.* **2021**, 60, 5245-5249.
(58) Wang, H.; Bian, Y. R.; Hu, J. T.; Dai, L. M. Highly crystalline sulfur-doped carbon nitride as photocatalyst for efficient visible-light hydrogen generation. *Appl. Catal. B-Environ.* **2018**, 238, 592-598.
(59) Liu, Z. F.; Huang, J.; Shao, B. B.; Zhong, H.; Liang, Q. H.; He, Q. Y.; Wu, T.; Pan, Y.; Peng, Z.; Yuan, X. Z.; Liu, Y.; Zhao, C. H. In-situ construc-

DOI: 10.14102/j.cnki.0254-5861.2022-0103

tion of 2D/1D $Bi_2O_2CO_3$ nanoflake/S-doped g-C_3N_4 hollow tube hierarchical heterostructure with enhanced visible-light photocatalytic activity. *Chem. Eng. J.* **2021**, 426, 130767.

(60) Li, X. B.; Xiong, J.; Gao, X. M.; Ma, J.; Chen, Z.; Kang, B. B.; Liu, J. Y.; Li, H.; Feng, Z. J.; Huang, J. T. Novel BP/BiOBr S-scheme nano-heterojunction for enhanced visible-light photocatalytic tetracycline removal and oxygen evolution activity. *J. Hazard. Mater.* **2020**, 387, 121690.

(61) Tahir, B.; Tahir, M. Synergistic effect of Ru embedded 2D Ti_3AlC_2 binary cocatalyst with porous g-C_3N_4 to construct 2D/2D Ru-MAX/PCN heterojunction for enhanced photocatalytic H_2 production. *Mater. Res. Bull.* **2021**, 144, 111493.

(62) Shen, R. C.; He, K. L.; Zhang, A. P.; Li, N.; Ng, Y. H.; Zhang, P.; Hu, J.; Li, X. In-situ construction of metallic Ni_3C@Ni core-shell cocatalysts over g-C_3N_4 nanosheets for shell-thickness-dependent photocatalytic H_2 production. *Appl. Catal. B-Environ.* **2021**, 291, 120104.

(63) Mahzoon, S.; Haghighi, M.; Nowee, S. M. Sonoprecipitation fabrication of enhanced electron transfer $Cu(OH)_2$/g-C_3N_4 nanophotocatalyst with promoted H_2 production activity under visible light irradiation. *Renew. Energy* **2020**, 150, 91-100.

(64) Feng, C. Y.; Tang, L.; Deng, Y. C.; Wang, J. J.; Liu, Y. N.; Ouyang, X. L.; Yang, H. R.; Yu, J. F.; Wang, J. J. A novel sulfur-assisted annealing method of g-C_3N_4 nanosheet compensates for the loss of light absorption with further promoted charge transfer for photocatalytic production of H_2 and H_2O_2. *Appl. Catal. B-Environ.* **2021**, 281, 119539.

(65) Fang, M.; Qin, Q.; Cai, Q.; Liu, W. Transparent Co_3FeO_x film passivated $BiVO_4$ photoanode for efficient photoelectrochemical water splitting. *Chin. J. Struct. Chem.* **2021**, 40, 1505-1512.

(66) Long, X. Y.; Meng, J. Z.; Gu, J. B.; Ling, L. Q.; Li, Q. W.; Liu, N.; Wang, K. W.; Li, Z. Q. Interfacial engineering of NiFeP/NiFe-LDH heterojunction for efficient overall water splitting. *Chin. J. Struct. Chem.* **2022**, 41, 2204046-2204053.

(67) Li, X. B.; Luo, Q. N.; Han, L.; Deng, F.; Yang, Y.; Dong, F. Enhanced photocatalytic degradation and H_2 evolution performance of NCDs/S-C_3N_4 S-scheme heterojunction constructed by π-π conjugate self-assembly. *J. Mater. Sci. Technol.* **2022**, 114, 222-232.

Received: May 1, 2022
Accepted: May 20, 2022
Published: June 20, 2022

DOI: 10.14102/j.cnki.0254-5861.2022-0103